Transport in the placenta: homogenizing haemodynamics in a disordered medium

By Igor L. Chernyavsky[1], Lopa Leach[2], Ian L. Dryden[3] and Oliver E. Jensen[1,*]

[1] School of Mathematical Sciences, University of Nottingham, University Park, Nottingham NG7 2RD, UK
[2] School of Biomedical Sciences, University of Nottingham, Queen's Medical Centre, Nottingham NG7 2UH, UK
[3] Department of Statistics, LeConte College, University of South Carolina, Columbia SC 29208, USA

The placenta is an essential component of the life-support system for the developing fetus, enabling nutrients and waste to be exchanged between the fetal and maternal circulations. Maternal blood flows between the densely packed branches of villous trees, within which are fetal vessels. Here we explore some of the challenges of modelling maternal haemodynamic transport using homogenization approaches. We first show how two measures can be used to estimate the minimum distance over which the distribution of villous branches appears statistically homogeneous. We then analyse a simplified model problem (solute transport by a unidirectional flow past a distribution of point sinks) to assess the accuracy of homogenization approximations as a function of governing parameters (Péclet and Damköhler numbers) and the statistical properties of the sink distribution. The difference between the leading-order homogenization approximation and the exact solute distribution is characterized by large spatial gradients at the scale of individual villi and substantial fluctuations that can be correlated over lengthscales comparable to the whole domain. This study highlights the importance of quantifying errors due to spatial disorder in multiscale approximations of physiological systems.

Keywords: placenta; homogenization; advection-diffusion-uptake; spatial point processes

1. Introduction

The placenta is a vital organ for the fetus. It performs multiple simultaneous functions, including exchange of blood gases between the maternal and fetal circulations and supply of nutrients to, and removal of waste products from, the fetus. In humans, where the embryo implants within the interstitium of the uterus, the placenta is highly invasive and haemochorial in organisation: in other words, maternal blood emerging from spiral arteries in the uterine wall flows freely around chorionic villous trees containing the fetal vessels [1, 2] (Figure 1(a)). This evolutionary strategy is
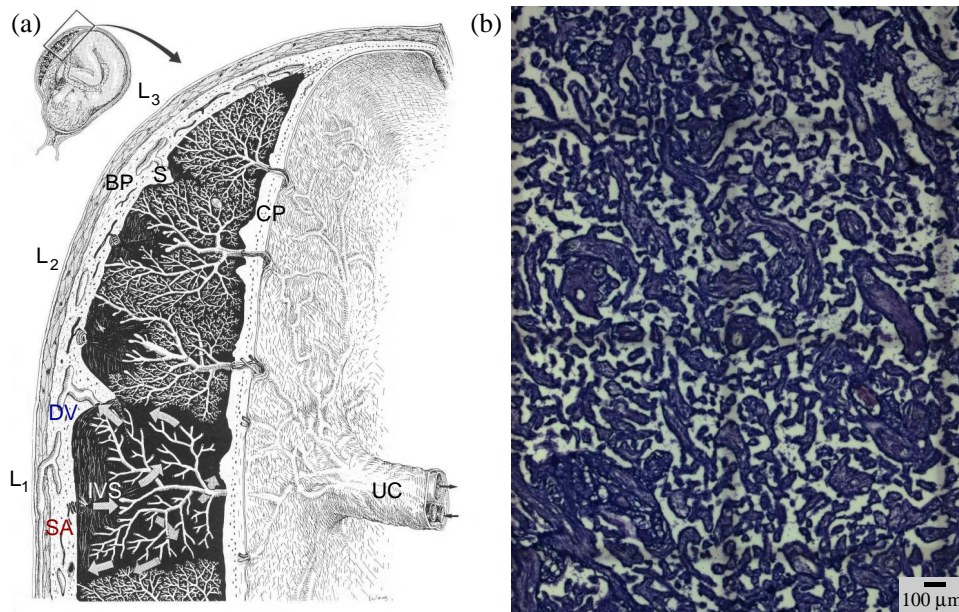
Figure 1. (*a*) Schematic diagram (modified from [2], with permission) of the nearly mature human placenta *in situ*, composed of the chorionic plate (CP) and the basal plate (BP) surrounding the intervillous space (IVS). The villous trees containing fetal vasculature (communicating with the fetus via the umbilical cord (UC)) project from the CP into the IVS and are directly surrounded by maternal blood that emerges from spiral arteries (SA) in the BP and circulates, as indicated by arrows in lobule L_1, to leave the IVS through the decidual veins (DV); terminal branches of the chorionic villi are not shown in L_1. Note the single villous tree in the peripheral lobule L_3, demarcated by the placental septum (S), as opposed to several trees in the central lobule L_2. (*b*) A cross-section of a normal peripheral placental lobule showing villous branches in the IVS (section taken parallel to the BP, 1mm from the decidua; optical magnification ×2.5).

shared between humans and only a few other species. The close maternal apposition makes human placental development and functioning vulnerable to maternal disease. For example, in pre-eclampsia (associated with intra-uterine growth restriction), inadequate invasion, raised maternal blood pressure and restricted maternal blood flow into the placenta are thought to impair development of fetal blood vessels and lead to reduced chorionic villous branching [3]. In maternal diabetes, there is increased angiogenesis and increased villous tree branching [4]. In either case, normal transport processes are compromised. Damage to the fetus during pregnancy can have immediate health implications as well as legacy effects which manifest in adulthood [5]. There are therefore obvious benefits in developing systems-level computational models of placental flow and transport that will help explain the origins and implications of structural abnormalities in disease, and help reveal the interactions between geometry, blood flow, growth and nutrient uptake that are central to the function of this organ.

    Despite its relative accessibility (using a freshly delivered term-placental perfu-

sion system) and its medical importance, theoretical models of placental function (summarized in [6]) remain relatively primitive. A particular challenge is the intricate geometrical structure of the villous trees (Figure 1(b)), which is hard to characterise, highly variable and prohibitively complex to simulate in detail. A natural starting point in modelling maternal placental blood flow is to exploit the theory of flow in porous media [7, 8]. We have recently used this approach to demonstrate the importance of the calibre of maternal spiral arteries and decidual veins in determining the overall flow resistance in a functional placental unit (or 'placentone,' containing a single villous tree) and to examine the factors that optimise nutrient delivery [6].

Behind porous medium models lies the theory of homogenization [9–11], which provides a systematic tool for characterising the bulk properties of materials in terms of their fine-scale structure. This method is particularly well developed for media with periodic microstructure. It is used for example to derive Darcy's law for viscous flow in a porous medium [12] and extensions that account for inertia [13] and poroelasticity [14]. In physiology, Darcy's law is widely used to simulate interstitial flows; it has also recently been applied to describe homogenized flow and transport within microcirculatory networks [15] when leakiness allows communication between nearby vessels. Through the use of volume-averaging procedures, approximations have also been developed for materials with random microstructure [16]. For materials with statistically homogeneous and ergodic microstructure, virtually all leading-order results for periodic media are directly applicable [12], including Darcy's law [17]; rigorous bounds on effective material properties for composite materials are available [12]. However fewer results are available connecting the statistical properties of the microstructure to the properties of the homogenization residue (the difference between the leading-order approximation and the exact solution) [18, 19].

In order to understand how the placenta functions as an organ of nutrient exchange, we here examine the combined effects of transport of solutes such as glucose or oxygen by maternal blood flow and uptake by the fetal circulation in villous trees. We can therefore call on prior studies [20–23] of the competition between advection, diffusion and reaction in porous media or heat exchangers, characterized by a Péclet number Pe (relating the strength of advection to diffusion) and a Damköhler number Da (relating the rate of reaction or uptake to diffusion). In addition to physical parameters, it is equally important to characterize the geometry of villous branches. Careful placental stereology (using systematic random sampling at the microscale) has provided estimates of bulk quantities (e.g. total villous volumes, surface areas and lengths) and local measures such as star volumes (the mean volume of all parts of a space which are visible when viewed in all directions from a given point within it) [24]. However further measures of placental anatomy, particularly of its statistical variability, are necessary in order to develop comprehensive models of placental transport.

In this paper, we draw together a number of techniques and ideas that are useful in developing multiscale stochastic models of nutrient transport in the human placenta. Using histological images (Figure 1(b)), we illustrate in §2(a) how methods of spatial statistics [25] can be used to characterize some of the important underlying lengthscales in villous trees. We then use an idealised theoretical model (transport under flow past a one-dimensional array of sinks, §2(b)) to assess how governing
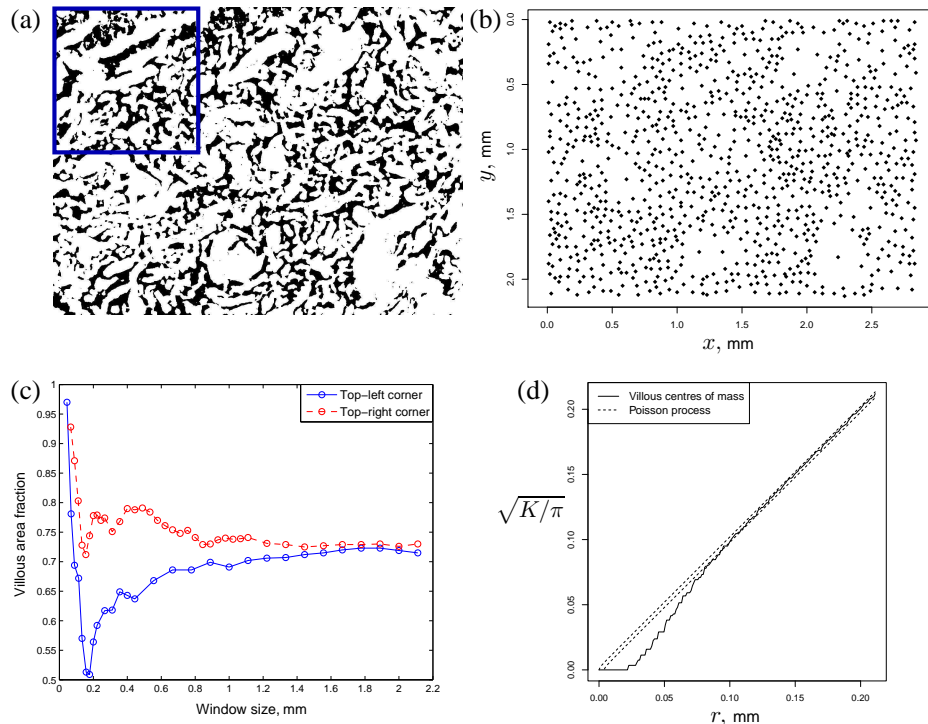
Figure 2. (*a*) An inverted rotated binary image of the cross-section shown in Figure 1(*b*), used to compute villous area fraction (the proportion of white space) in an observation window (solid square (top left) indicates the window size of about 1 mm); (*b*) the corresponding spatial point process generated by the centres of mass of villous cross-sections (after despeckling and watershedding, $N = 976$ points); (*c*) dependence of villous area fraction ϕ on window size W, taken from the top-left (solid) and top-right (dashed) corners of the sample in (*a*); (*d*) square root of the corresponding K-function (2.3) (solid) *vs.* correlation distance r; dashed lines indicate 95%-confidence interval (± 2 standard errors) for the K-function of a Poisson process, computed using (2.4).

parameters (Pe, Da) and the statistical properties of the sink distribution together affect the accuracy of homogenization approximations (§2(*c, d*)). We show in particular how randomness leads to large fluctuations in solute distributions that can be correlated over surprisingly long distances.

2. Methods

(*a*) *Imaging and spatial statistics*

A peripheral lobule of the human placenta was used for the histological study, as it tends to contain a single chorionic villous tree matched with a spiral artery, and is therefore more representative of a single placental circulatory unit [2, 6]. A single maternal lobule, obtained from a normal full-term placenta (delivered by elective

cesarian section), was frozen in nitrogen-cooled isopentane before cutting according to a systematic random sampling protocol. 8μm-thick sections were stained with tolonium chloride (Toluidine Blue), revealing the chorionic villi and the medium-to-large blood vessels within them. An example is shown in Figure 1(b), using QImaging MicroPublisher 5 Mpx camera and a Zeiss Axioplan microscope. We used `ImageJ` to identify villous branch outlines (Figure 2(a)) and compute their area fraction ϕ as a function of window size W [26]. Centres of mass of each branch (Figure 2(b)) enable us to interpret villous branch locations as a spatial point process to which we can apply appropriate statistical methodology [25].

Let $N(A)$ represent the number of points lying within an area A. The first- and second-order intensities of this process are

$$\lambda(\mathbf{x}) = \frac{\mathbb{E}[N\{\,\mathrm{d}A(\mathbf{x})\}]}{|\,\mathrm{d}A(\mathbf{x})|}, \quad \lambda_2(\mathbf{x}_1, \mathbf{x}_2) = \frac{\mathbb{E}[N\{\,\mathrm{d}A(\mathbf{x}_1)\}N\{\,\mathrm{d}A(\mathbf{x}_2)\}]}{|\,\mathrm{d}A(\mathbf{x}_1)||\,\mathrm{d}A(\mathbf{x}_2)|}. \tag{2.1}$$

in the limit $|\,\mathrm{d}A(\mathbf{x})| \to 0$, where $\mathrm{d}A(\mathbf{x})$ is an infinitesimal area around a given point $\mathbf{x}$. The density λ is the expected number of points per unit area. The two-point correlation function λ_2 is the normalised joint number of points expected around two given points in space. For a stationary isotropic point process, for which $\lambda = \mathrm{constant}$, $\lambda_2(\mathbf{x}_1, \mathbf{x}_2) = \lambda_2(|\mathbf{x}_1 - \mathbf{x}_2|)$ [12]. The K-function [25] is the average number of points within a given distance r from an arbitrary point $\mathbf{x}_0$, scaled with λ, where

$$K(r) = \frac{1}{\lambda}\mathbb{E}[N\{\mathbf{x} : |\mathbf{x} - \mathbf{x}_0| \le r\}] = \frac{2\pi}{\lambda^2} \int_0^r \lambda_2(t)t\,\mathrm{d}t. \tag{2.2}$$

For a completely random spatial point (Poisson) process, $K = \pi r^2$ and $\lambda_2 = \lambda^2$. For n points in a given rectangular domain of area $|A|$ and perimeter P (as in Figure 2(b)), we employ Ripley's estimate $\hat{K}$ for the K-function defined as

$$\hat{K}(r) = \frac{|A|}{n(n-1)} \sum_{\substack{i,j=1 \\ (i \ne j)}}^{n} w_{ij}^{-1}\mathrm{I}(|\mathbf{x}_i - \mathbf{x}_j| \le r), \tag{2.3}$$

where I is an indicator function and w_{ij} is Ripley's trigonometric weighting function to correct for edge effects [25].

We use the K-function to estimate the cross-correlation of intervillous distances and to test the pattern for regularity or clustering, as compared to the complete spatial randomness represented by a Poisson point process [25]. For the latter, we use

$$\mathbb{E}[\hat{K}_{\mathrm{Poisson}}] = \pi r^2, \quad \mathrm{Var}[\hat{K}_{\mathrm{Poisson}}] = |A|^2 \frac{(2b(r) - a_1(r) + (n-2)a_2(r))}{n(n-1)}, \tag{2.4}$$

where $a_1(r) = |A|^{-2}(0.21Pr^3 + 1.3r^4)$, $a_2(r) = |A|^{-3}(0.24Pr^5 + 2.62r^6)$ and $b(r) = \pi r^2|A|^{-1}(1 - \pi r^2|A|^{-1}) + |A|^{-2}(1.0716Pr^3 + 2.2375r^4)$ are Lotwick and Silverman's polynomials [27]. We estimate $\hat{K}$ in (2.3) and (2.4) using the `Kest` function of the `Spatstat` package for `R` [28]; (2.4b) is exact for r not exceeding 1/4 of the

smallest side of a rectangular domain [27]. Measurements of area fraction ϕ and the K-function for placental tissue are discussed in §3(*a*) below.

(*b*) *A model problem for solute uptake*

As a simple representation of solute uptake by a villous tree, such as within lobule L_1 in Figure 1(*a*), we consider a one-dimensional array of N identical point sinks of strength q_0, distributed across a domain $0 \leq x^* \leq L$. The distance L represents a typical pathlength between spiral artery and decidual vein, passing multiple villous trees; for example see [6]. The typical distance between two adjacent sinks is $l = L/(N+1)$ and we assume $\varepsilon \equiv l/L \ll 1$. A solute with steady concentration distribution $C^*(x^*)$ is swept past the sinks by a uniform flow field u_0 and diffuses between them with diffusion coefficient D; the concentration C_0 at the inlet (representing a spiral artery) is prescribed and the concentration at the outlet is set to be zero. The concentration field is assumed non-negative, so that if q_0 is sufficiently large an internal free boundary at $x^* = x_0^*$ arises such that $C^* > 0$ for $0 < x^* < x_0^*$, and $C^* = 0$ for $x_0^* \leq x^* \leq L$. Writing $C^*(x^*) = C_0 C(x)$, $x^* = lx$, $x_0^* = lx_0$, the dimensionless solute distribution satisfies

$$\mathrm{Pe}C_x = C_{xx} - \mathrm{Da}f(x) \quad \text{for} \quad 0 \leq x \leq \min(x_0, \varepsilon^{-1}), \qquad (2.5a)$$

$$C(0) = 1, \qquad (2.5b)$$

$$C(\varepsilon^{-1}) = 0 \quad \text{or} \quad C(x_0) = C_x(x_0) = 0 \text{ for } 0 < x_0 < \varepsilon^{-1}, \qquad (2.5c)$$

where $\mathrm{Pe} = u_0 l/D$ is a Péclet number and $\mathrm{Da} = q_0 l/(DC_0)$ a Damköhler number, each defined using the inter-sink distance. Solute uptake is assumed to follow zeroth-order kinetics, the sinks being represented by

$$f(x) = \sum_{i=1}^{N} \delta(x - \xi_i) \qquad (2.6)$$

for the ordered sink locations $0 < \xi_1 < \xi_2 < \cdots < \xi_N < 1$. For convenience we define $\xi_0 = 0$ and $\xi_{N+1} = 1$ and define $\Delta_i \equiv \xi_i - \xi_{i-1}$ $(i = 1, \ldots, N+1)$.

Motivated by the spatial patterns in Figure 2(*b*), we consider four sink distributions, allowing us to mimic structural features that are potentially of relevance to villous trees:

(i) $f = f_p$, say, a periodic distribution with $\xi_i = i$, $\Delta_i = 1$ for $1 \leq i \leq N$;

(ii) $f = f_u$, say, a uniformly random distribution where ξ_i are ordered values drawn from independent $\mathcal{U}[0, \varepsilon^{-1}]$ distributions, implying $\varepsilon\xi_i \sim \mathrm{Beta}(i, N + 1 - i)$ and $\varepsilon(\Delta_1, \ldots, \Delta_N) \sim \mathrm{Dirichlet}(\boldsymbol{\xi}|\boldsymbol{\alpha})$ where $\boldsymbol{\xi} = (\xi_1, \ldots, \xi_N)$ and $\boldsymbol{\alpha} = (1, 1, \ldots, 1) \in \mathbb{R}^N$ [29];

(iii) $f = f_h(d)$, say, a Matérn hard-core type-II distribution, whereby sinks are drawn sequentially from a uniformly random distribution and are accepted provided they do not fall within a distance d of an existing sink or boundary, the process being continued until N sinks are reached [25];

(iv) $f = f_n(\sigma)$, say, a normally-perturbed periodic distribution satisfying $\xi_i \sim \mathcal{N}(i, \sigma^2)$, for some variance σ^2, with periodic conditions imposed on sinks

falling outside the domain. Sinks are reordered if they swap positions (as occurs for sufficiently large σ).

In the limit $d \rightarrow 0$, f_h tends to f_u; in the limit $d \rightarrow d_{\mathrm{cr}}$, f_h exhibits increasing regularity, where d_{cr} is an upper bound estimated empirically to be close to $\pi/\sqrt{18} \approx 0.74$ [30]. All distributions have the first-order intensity $\lambda = 1$. The population autocorrelation of the inter-sink distance, defined by

$$\mathcal{R}_\Delta(n) = \frac{\mathbb{E}\left[(\Delta_i - \mathbb{E}[\Delta_i])(\Delta_{i+n} - \mathbb{E}[\Delta_{i+n}])\right]}{\mathrm{Var}[\Delta_i]}, \tag{2.7}$$

satisfies $\mathcal{R}_\Delta(n) = 0$ for $n > 0$ and small σ for $f = f_n$ (reflecting independent sink locations) and (using standard properties of Dirichlet distributions [31]) $\mathcal{R}_\Delta(n) = -1/(N+2)$ for $n > 0$ for $f = f_u$ (i.e. a large gap between sinks is compensated by reduced gaps elsewhere); simulations (taking the mean from an ensemble of realisations of each process) confirm that $\mathcal{R}_\Delta(n) \lesssim n^{-1}$ for all three random distributions (when $d = 0.65$, $\sigma = 10$, data not shown), implying that there is no substantial long-scale correlation in the sink distributions.

We simulate realisations of each distribution and compute the transport problem (2.5) over each distribution using a semi-analytical method, matching concentration fluxes at each sink. Mesh convergence was checked by validation against the results obtained by the finite-element solver COMSOL Multiphysics and exact solutions in simple cases. Results are presented in §3(b, c) below, tested against predictions from homogenization approximations that we now develop for periodic and random sink distributions.

(c) *Homogenization approximation: periodic sinks*

We develop asymptotic approximations of (2.5) in the limit $\varepsilon \rightarrow 0$ using homogenization. When $f = f_p$ a standard approach may be adopted, described in Appendix A, the outcomes of which we summarize briefly here. The concentration field is represented by a two-scale expansion of the form $C(x) = C^{(0)}(X) + \varepsilon C^{(1)}(x, X) + \varepsilon^2 C^{(2)}(x, X) + \ldots$, where $X = \varepsilon x$ characterises the slow variation of the solution over lengthscales comparable to the whole domain, while x characterises rapid variations over a 'unit cell' surrounding an individual sink.

Key features of the concentration field over a periodic distribution of sinks are summarised in Figure 3. Diffusive, advective and uptake fluxes across the whole domain balance when $DC_0/L \sim u_0 C_0 \sim q_0 N$, which corresponds to $\mathrm{Da} = O(\varepsilon^2)$, $\mathrm{Pe} = O(\varepsilon)$. For given ε, this defines an organising centre in $(\mathrm{Pe}, \mathrm{Da})$-parameter space (Figure 3(a)). A second organising centre lies at $\mathrm{Pe} = O(1)$, $\mathrm{Da} = O(\varepsilon)$. By deriving distinct asymptotic limits for C around each organising centre, we can obtain a comprehensive overview of the homogenization approximation across parameter space. This provides useful perspective before focusing on parameters appropriate for specific solutes.

We first set $\mathrm{Pe} = \varepsilon p$, $\mathrm{Da} = \varepsilon^2 q$ and assume $p, q = O(1)$ as $\varepsilon \rightarrow 0$. $C^{(0)}$ then satisfies $pC_X^{(0)} = C_{XX}^{(0)} - q$ (see (A 5)). The two-parameter solution for $C^{(0)}$ (given by (A 6)) encompasses four distinct limits, denoted U_A, U_D, D, and A in Figure 3(a), in which different physical effects dominate. Representative solutions, illustrating the

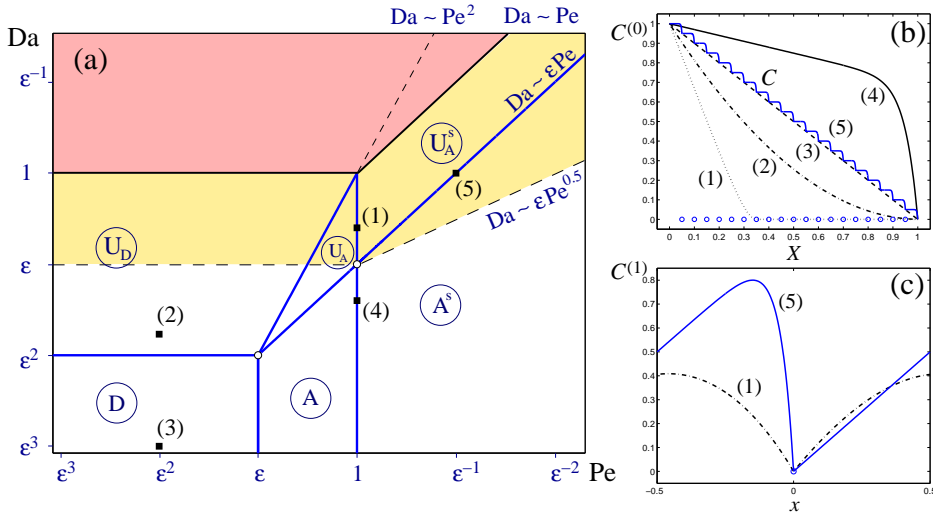Figure 3. (a) Asymptotic regimes in $(\mathrm{Pe}, \mathrm{Da})$-parameter space for transport past a periodic sink distribution with $\varepsilon \ll 1$. Solid lines demarcate six distinct regions (uptake-dominated $\mathrm{U_D}$, $\mathrm{U_A}$, $\mathrm{U_A^s}$; diffusion-dominated D; advection-dominated A, $\mathrm{A^s}$). The lightly shaded region above the dashed lines indicates the domain of weak convergence of the homogenization approximation to the exact solution (in the L_2 but not the H^1 norm); the homogenization approximation fails in the darker shaded region for large Da. (b) Concentration profiles (A 6a) for representative points (1)-(5) in the parameter space ($\mathrm{Pe} = 1, \varepsilon^2, \varepsilon^2, 1, \varepsilon^{-1}$ and $\mathrm{Da} = \varepsilon^{0.6}, 2\varepsilon^2, \varepsilon^3, \varepsilon^{1.4}, 1$ respectively), showing the leading-order approximation $C^{(0)}$ (1-4) and the full solution (5) computed with $\varepsilon = 0.05$; circles show the locations of the 19 sinks. (c) Corrections $C^{(1)}$ given by (A 12a) at points (1) and (5), within a unit cell with the sink at $x = 0$.

form of $C^{(0)}$ in each region of $(\mathrm{Pe}, \mathrm{Da})$-parameter space, are shown in Figure 3(b) at points (1), (2), (3), (4) respectively. Briefly:

- in region D ($p \ll 1$, $q \ll 1$, illustrated by point (3)), $C^{(0)} \approx 1 - X$, representing diffusion between the boundary source and sink, the distributed sinks and advection being too weak to have any effect at leading order;

- in region $\mathrm{U_D}$ ($p \ll 1$, $\max(1, p^2) \ll q \ll \varepsilon^{-2}$, illustrated by point (2)), $C^{(0)} \approx (1 - (X/X_0))^2$ for $0 \leq X \leq X_0 = \sqrt{2/q} \ll 1$ and $C^{(0)} = 0$ otherwise, representing uptake by the distributed sinks balancing diffusion;

- in region $\mathrm{U_A}$ ($1 \ll p \ll \varepsilon^{-1}$, $p \ll q \ll p^2$, illustrated by point (1)), $C^{(0)} \approx 1 - (X/X_0) - (1/pX_0)\mathrm{e}^{-p(X_0 - X)}$ for $0 \leq X \leq X_0$, with $\varepsilon \ll X_0 \approx p/q \ll 1$, representing uptake by the distributed sinks balancing advection (outside a diffusive boundary layer near $X = X_0$);

- in region A ($1 \ll p \ll \varepsilon^{-1}$, $q \ll p$, illustrated by point (4)), $C^{(0)} \approx 1 - \mathrm{e}^{-p(1 - X)}$, representing dominant advection, supplemented by diffusion close to the outlet.

Article submitted to Royal Society

In the neighbourhood of $\mathrm{Pe} = O(\varepsilon)$, $\mathrm{Da} = O(\varepsilon^2)$, the first correction $\varepsilon C^{(1)}$ vanishes, while the second correction $\varepsilon^2 C^{(2)}$ (see (A 8)) is proportional to Da. This rises to $O(\varepsilon)$ as Da approaches $O(\varepsilon)$, violating the assumed structure of the original asymptotic expansion, and indicating breakdown of the homogenization approximation along $\mathrm{Pe} \ll 1$, $\mathrm{Da} = O(1)$. Furthermore, the correction within the unit cell develops an internal boundary layer (in x) of width $1/\mathrm{Pe}$ adjacent to the sink as Pe increases through unity (compare points (1) and (5), Figure 3(c)), signalling the development of 'staircases' in the concentration profile, occuring in regions A^s and U_A^s in (Pe, Da)-space (Figure 3(a, b)). To capture these, a new expansion must be constructed near the second organising centre at $\mathrm{Pe} = O(1)$, $\mathrm{Da} = O(\varepsilon)$. Writing $\mathrm{Da} = \varepsilon q_1$ with $q_1 = O(1)$ as $\varepsilon \to 0$, we find that here $C^{(0)}$ decreases linearly from the inlet (see (A 10)), before terminating in a diffusive boundary layer either upstream of, or at, the downstream boundary (illustrated respectively by points (1) and (4) in Figure 3b); the correction $C^{(1)}$ satisfies (A 12).

To assess the difference between the leading-order homogenized and exact solutions to (2.5), we define the homogenization residue (or corrector) as

$$r^\varepsilon \equiv C(x) - C^{(0)}(X). \tag{2.8}$$

For periodic sink distributions, we estimate the residue using $r^\varepsilon \approx \varepsilon C^{(1)}$ for $\mathrm{Pe} = O(1)$ (and $r^\varepsilon \approx \varepsilon^2 C^{(2)}$ for $\mathrm{Pe} = O(\varepsilon)$) and assess its magnitude under the (weak) mean-squared and (strong) Sobolev norms:

$$\|f(X)\|_{L_2}^2 \equiv \int_0^1 f^2 \, \mathrm{d}X, \quad \|f(X)\|_{H^1}^2 \equiv \|f\|_{L_2}^2 + \|f_X\|_{L_2}^2. \tag{2.9}$$

The convergence of $C^{(0)}$ to C across parameter space is discussed in §3(b) below.

(d) Homogenization approximation: random sink distributions

For the random sink distributions ($f = f_u$, f_h or f_n in (2.5)), the same leading-order problem (A 5) for $C^{(0)}$ emerges. This is readily shown via averaging over long spatial scales, following [32]. Thus we can again make direct use of the parameter-space map in Figure 3(a).

We use two approaches to determine the size and statistical properties of the residue (2.8). When $\mathrm{Pe} = O(\varepsilon)$ and $\mathrm{Da} = O(\varepsilon^2)$ (and diffusion dominates advection at the microscale), we can determine the statistics of r^ε directly (see Appendix B). The fluctuations r^ε are related to linear combinations of the sink locations ξ_i, weighted by the slowly varying coordinate X. Evaluation of $\mathbb{E}(r^\varepsilon)$ (see (B 9)) yields the homogenized ODE (A 5a), while we find that the pointwise variance satisfies

$$\mathrm{Var}(r^\varepsilon) \approx \begin{cases} \varepsilon^3 \sigma^2 q^2 X(1-X) & \text{for} \quad f = f_n, \sigma = O(1), \\ \frac{1}{12}\varepsilon q^2 X^2 (1-X)^2 & \text{for} \quad f = f_u. \end{cases} \tag{2.10}$$

(The equivalent expression for $f = f_h$ is harder to obtain and is left for further work.) The variance varies smoothly with X, vanishing at either end of the domain where the concentration is prescribed. When the sinks are almost periodic ($f = f_n$

in (2.10)), fluctuations about $C^{(0)}$ are of magnitude $O(\varepsilon^{3/2})$ (in the L_2 norm), whereas these rise substantially (to $O(\varepsilon^{1/2})$) when there is greater disorder in the sink locations ($f = f_u$).

For larger Pe, we compute r^ε for $f = f_u$, f_h and f_n using Monte Carlo simulations of (2.5). We estimate its convergence in mean $\mathbb{E}[\|r^\varepsilon\|_{L_2}]$ by evaluating integrals with trapezium quadrature. We also estimate $\mathrm{Var}(r^\varepsilon)$ and the transverse covariance

$$\mathrm{Cov}_T(r^\varepsilon(x)) \equiv \mathbb{E}\left[(r^\varepsilon(x) - \mathbb{E}[r^\varepsilon(x)])\left(r^\varepsilon(\varepsilon^{-1} - x) - \mathbb{E}[r^\varepsilon(\varepsilon^{-1} - x)]\right)\right], \qquad (2.11)$$

which characterises the degree to which fluctuations are correlated across the domain. Results are presented in §3(c) below.

3. Results

(a) *Imaging*

Figure 2(c) shows how the villous area fraction ϕ depends on the size W of the window used to compute it. When W is comparable to the diameter of terminal villi (below 100 μm), we see vigorous oscillations of ϕ, depending whether the window falls in villous tissue or intervillous space. As W increases, variations in ϕ fall and are significantly reduced for $W \gtrsim 1$ mm. Above this threshold, we can reasonably treat the intervillous space in this sample as a continuous medium of uniform (or at least slowly varying) area fraction, as was assumed in [6] for example.

In Figure 2(d), the estimated K-function (2.3) for the distribution of centres of villous branches is compared to that expected of a homogeneous Poisson process (with confidence intervals). The two are indistinguishable, for the given sample, at inter-point distances $r \gtrsim 0.1$mm. Figure 2(d) also shows that no points fall within approximately 25μm of each other and that, for $r < 0.1$mm, points are more regular than they would be if distributed uniformly randomly (resembling a hardcore process). This in part reflects the finite size of terminal villous branches, of typical diameter 50μm (Figure 1(b)).

(b) *Accuracy of the homogenization approximation for periodic sink distributions*

We now explore how the spatial distribution of villous branches, represented by point sinks in (2.5), the strength of flow past these sinks (represented by Pe) and the sink strength (represented by Da) together determine patterns of uptake. The placenta acts as exchange organ for numerous different solutes, each of which is characterized by its own values of Pe and Da. We wish to assess the accuracy of the leading-order homogenization approximation $C^{(0)}$ across parameter space.

We first review concentration profiles over a periodic array (Figure 3). For given Pe, there is a critical Da (see (A 6b)), equivalent to

$$\mathrm{Da}_{\mathrm{cr}}(\mathrm{Pe}) = \frac{\mathrm{Pe}^2 \mathrm{e}^{\mathrm{Pe}/\varepsilon}}{(\mathrm{Pe}/\varepsilon - 1)\mathrm{e}^{\mathrm{Pe}/\varepsilon} + 1}, \qquad (3.1)$$

such the solute is fully absorbed within the domain (i.e. for $X \leq X_0 < 1$) for Da $>$ $\mathrm{Da}_{\mathrm{cr}}(\mathrm{Pe})$. This threshold in (Pe, Da)-space asymptotes to the boundary between

asymptotic regions U and U_D for Pe $\ll \varepsilon$ (when $\mathrm{Da}_{cr} \approx 2\varepsilon^2$) and the boundary between regions A and U_A (and A_S and U_A^S) for Pe $\gg \varepsilon$ (when $\mathrm{Da}_{cr} \approx \varepsilon$Pe). Thus (3.1) demarcates a region where uptake by sinks can be considered optimal: for $\mathrm{Da} > \mathrm{Da}_{cr}$, all the solute is absorbed upstream of the outlet, making some sinks redundant; for $\mathrm{Da} < \mathrm{Da}_{cr}$, substantial solute escapes past the sinks to the outlet. Of particular relevance for common nutrients such as glucose and oxygen in the placenta is the regime in which Pe is order unity or larger [6], which we illustrate using point (5) in Figure 3. In this case the correction to $C^{(0)}$ develops an internal boundary-layer within each unit cell. For sufficiently large Da and Pe, this leads to a 'staircase' structure in the exact solution (Figure 3(b, c)). Leading-order solute distributions, such as those computed in [6], fail to capture these significant local variations in the solute field.

We now survey (Pe, Da)-space to assess regimes of weak or strong convergence of the residue (2.8) (i.e. $\|r^\varepsilon\|_{L_2} \to 0$ or $\|r^\varepsilon\|_{H^1} \to 0$ as $\varepsilon \to 0$ respectively). For Pe $\ll 1$, we find that $\|r^\varepsilon\|_{L_2} = O(\mathrm{Da})$ and $\|r^\varepsilon\|_{H^1} = O(\mathrm{Da}/\varepsilon)$ (using (A 8)), implying strong convergence for Da $\ll \varepsilon$. This reveals a region of parameter space (Pe $\ll 1$, $\varepsilon \ll$ Da $\ll 1$) where the correction to $C^{(0)}$, while bounded, has large gradient. For Pe $\gg 1$, we find that $\|r^\varepsilon\|_{L_2} = O(\mathrm{Da}/\mathrm{Pe})$ and $\|r^\varepsilon\|_{H^1} = O(\mathrm{Da}/\varepsilon\sqrt{\mathrm{Pe}})$ (using (A 13)), implying strong convergence for Da $\ll \varepsilon\sqrt{\mathrm{Pe}}$. We can therefore split (Pe, Da)-space into three regions (Figure 3(a)): in the unshaded region below the dashed line there is strong convergence of the homogenization approximation; the weakly shaded region above the dashed line is characterised by weak convergence in which $C^{(0)}$ fails to capture large gradients at the microscale; and the homogenization approximation fails in the dark-shaded region at large Da. In the regime of particular physiological significance (point (5)), convergence is weak.

(c) *Accuracy of the homogenization approximation for random sink distributions*

The homogenised leading-order solution (A 6a) is applicable not only to a periodic array but also for a statistically homogeneous random distribution of sinks of the same average density. We now test it against simulations using the three stochastic sink distributions described in §2(b): a uniformly random distribution (f_u), a Matérn hard-core distribution (f_h) and a perturbed periodic distribution (f_n).

We consider point (5) in Figure 3(a), for which $C^{(0)} = 1 - X$. As advection dominates diffusion at the microscale, the exact solution for any realisation of the sink distribution becomes an irregular staircase, exhibiting distinct plateaux between clusters of sinks. Even though the sink distributions are stationary processes that are not correlated over multiple sinks (§2(d)), the residues r^ε for $f = f_u$ and f_h (Figure 4(a, b, d, e)) show long-scale correlation: the variance is proportional to $X(1-X)$ and the transverse covariance (proportional to X^2 in $0 < X < \frac{1}{2}$ and $(1-X)^2$ in $\frac{1}{2} < X < 1$) suggests that fluctuations are correlated over lengthscales comparable to the full domain, the correlation being greatest away from boundaries. r^ε for $f = f_n$ with $\sigma = 10$ also shows evidence of long-scale correlation (Figure 4(c, f)); in this case the variance and transverse covariance are approximately uniform across the domain (outside boundary layers at $X = 0$ and $X = 1$).

Figure 4(g, h) shows how the magnitude of the residue depends on d (for f_h) and σ (for f_n), for different values of ε. (Recall that for $d = 0$, f_h is equivalent to f_u,
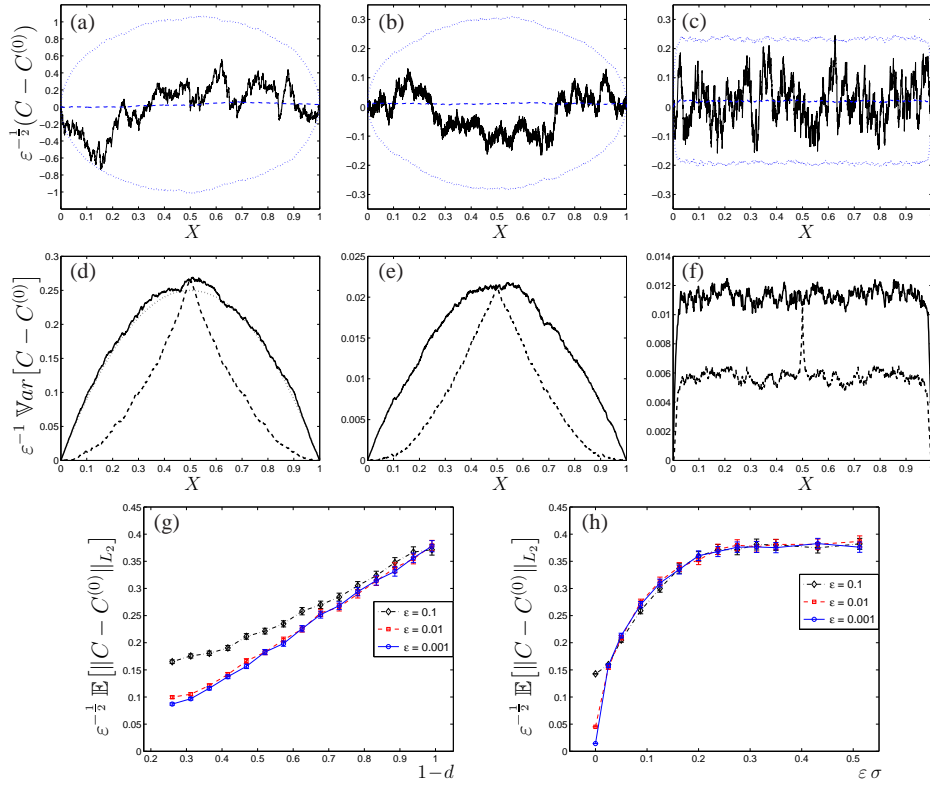
Figure 4. (a–c) Homogenization residue $r^\varepsilon = C - C^{(0)}$ (solid) scaled by $\varepsilon^{-1/2}$ for (a) uniformly random, (b) hard-core ($d = 0.65$) and (c) normally perturbed ($\sigma = 10$) point processes for $\varepsilon = 0.001$, Pe $= 10$, Da $= \varepsilon$Pe. Dashed line shows population mean from $n = 1000$ samples, dotted line shows mean $\pm$ two standard deviations. (d–f) Variance (solid) and transverse covariance (2.11) (dashed), scaled with ε^{-1}, corresponding to (a-c) (the dotted line shows $X(1-X)$ in (d)). (g, h) Dependence of homogenization error (estimated from $n = 1000$ samples) on the minimal inter-sink distance d for $f = f_h$ (g) and on the standard deviation σ for $f = f_n$ (h) (scaled by $\varepsilon^{-1/2}$ for $\varepsilon = 0.1, 0.01, 0.001$; Pe $= 10$, Da $= \varepsilon$Pe). Error bars are ± 2 standard errors (SE), where SE $= \sqrt{\mathrm{Var}(\|r^\varepsilon\|_{L_2})/n}$, calculated using a standard unbiased estimate.

and that f_n resembles f_u for sufficiently large σ.) Collapse of the data for different ε indicates that in both cases the residue $\mathbb{E}(\|r^\varepsilon\|_{L_2})$ is $O(\varepsilon^{1/2})$ for sufficiently small d and sufficiently large σ (as expected from [18]), although the error falls in magnitude as the distributions become more regular (either by increasing d towards d_{cr} or reducing σ close to zero). Indeed for $\sigma = 0$ the residue has exactly the scaling predicted by asymptotics for the periodic sinks, namely $\|r^\varepsilon\|_{L_2} \approx 0.451\varepsilon$ (for Pe $= 10$, Da $= \varepsilon$Pe). The magnitude of the residue approaches the value of the uniformly random distribution for $\varepsilon\sigma \gtrsim 0.3$.

When diffusion dominates at the microscale (Pe $= O(\varepsilon)$, Da $= O(\varepsilon^2)$), the pointwise variance again varies smoothly over the whole domain, as we show ana-

lytically in (2.10) (see also Appendix B). However its magnitude depends strongly on the degree of periodicity in the underlying structure, with fluctuations rising from $O(\varepsilon^{3/2})$ for almost periodic sink distributions to $O(\varepsilon^{1/2})$ for uniformly random sink distributions. Correspondingly, the range of validity of the homogenization approximation when $f = f_u$ is significantly smaller than in the periodic case: we estimate that this requires $\mathrm{Da} \ll \varepsilon^{3/2}$ for $\mathrm{Pe} \ll \varepsilon$ and $\mathrm{Da} \ll \varepsilon^{1/2}\mathrm{Pe}$ for $\mathrm{Pe} \gg \varepsilon$.

4. Discussion

Heterogeneous and disordered biological media such as the human placenta require careful consideration of statistical variability when simulating transport processes, both in characterising the underlying geometry and in understanding the impact of randomness on physical processes. Regarding the former, we have illustrated how sampling villous area fraction and estimation of the K-function (Figure 2(c, d)) reveal important intrinsic lengthscales in the distribution of villous branches. For the sample considered, our data show no evidence against uniformly random distributions patterns of villous trees over sufficiently large distances and no evidence of underlying periodicity that would give rise to clear steps in the K-function [33]. The K-function instead resembles a hard-core distribution at shorter lengthscales (Figure 2(d)), consistent with the requirement that branches cannot overlap. Further development of semi-automated image analysis, e.g. in watershedding segmentation algorithms [26], should allow bulk processing of histological data and reduce systematic errors. Future studies can be used to fit parameters of suitable spatial models to histological data and to assess how these features of tissue architecture may vary during development, in disease and between individuals.

In the absence of highly resolved measurements of maternal blood flow and solute distributions within the intervillous space, we chose here to examine nutrient transport using a simple theoretical model that incorporates spatial disorder in sink distributions. The model ignores many important features of placental haemodynamics, such as the finite size of villous branches, complex uptake kinetics for specific nutrients (glucose, amino acids, lipids etc.) that may be mediated by active transport mechanisms in the syncytiotrophoblast on the outer surface of villous branches [34], the non-Newtonian rheology of flow in intervillous space (and the associated hematocrit distributions, that would determine the oxygen-carrying capacity of maternal blood), higher-dimensional transport processes such as Taylor dispersion [35], flow and tissue inhomogeneities (for example near spiral artery outlets [6]) and distortion of villous branches by flow. It is important that future transport models including each of these refinements are evaluated against data as they become available. Instead we have used our simplified model to illustrate some generic features of homogenization approximations for disordered media, which we hope will provide a useful foundation for more sophisticated simulations of placental function.

While periodic or random sink distributions share similar leading-order approximations (through the slowly varying concentration field $C^{(0)}(X)$), the accuracy of this approximation depends on parameter values (Pe, Da and ε) and sink statistics. We classified asymptotic parameter regimes in (Pe, Da)-space (Figure 3(a)), in which different balances between diffusion, advection and uptake are locally dominant at the macroscale. For the regime of greatest interest physiologically (point

(5)), convergence of $C^{(0)}$ to the exact solution is weak (applying in the L_2 but not the H^1 norm), because corrections have large spatial gradients on lengthscales below the inter-sink distance. Such fine-scale features, not captured by leading-order homogenization, are likely to be of importance in models that resolve the detailed arrangement of fetal vessels within villous branches.

The magnitude of the difference between the homogenization approximation and the exact solution depends on how one chooses to measure it. In a weak (L_2) norm, the residue with a periodic sink distribution is typically $O(\varepsilon)$ (for example for Pe $= O(1)$, Da $= O(\varepsilon)$), falling to $O(\varepsilon^2)$ at sufficiently low Pe and Da. However when sinks have a uniformly random distribution, the residue (in the appropriate norm) rises to $O(\varepsilon^{1/2})$ in both cases ((2.10), Figure $4(a, b)$). The magnitude of the residue falls for distributions with a greater degree of periodicity ((2.10), Figure $4(g, h)$) but grows with increasing sink strength. Significantly, even when sink distributions are correlated only over short distances, the residues appear to be correlated over distances comparable with the domain size when advection dominates at the macroscale (figure $4(d, e, f)$). This is also the case when diffusion dominates at the microscale, as revealed by estimates of the transverse covariance (data not shown). While the distribution of villous branches in a placental unit (Figure 2) is significantly more complex than the simple distributions employed in Figure 4, one can estimate ε crudely to be between 0.001 and 0.01, suggesting errors in homogenization approximations due to stochasticity of up to 10% that fluctuate across distances comparable to an individual lobule.

Homogenization approaches provide a powerful tool in multiscale modelling and are likely to figure prominently in future integrative models of other tissues with fine-grained periodic or random microstructure (such as the liver [36]). However this study shows the merits of stepping beyond the leading-order approximation in order to resolve fine-scale structures at the microscale and, perhaps more importantly, to assess carefully the magnitude and nature of cumulative (and parameter-dependent) errors that arise from stochastic variation. These errors must be interpreted using the language of non-smooth functions and distributions. Such steps will be particularly important when building complex models that integrate numerous competing processes, in order to avoid errors arising at each level of approximation from accumulating and disrupting the overall predictive capacity of the model.

Appendix A. Homogenization for periodic sink distributions

We seek solutions of (2.5) in the form $C(x) = \tilde{C}(x, X)$, introducing a slowly varying spatial variable $X = \varepsilon x$ that becomes independent of x as $\varepsilon \to 0$ (at least in a sense of weak two-scale convergence [11]), allowing derivatives to be expressed as

$$\frac{\mathrm{d}}{\mathrm{d}x} = \frac{\partial}{\partial x} + \varepsilon \frac{\partial}{\partial X}. \tag{A 1}$$

We further assume that $\tilde{C}(x, X)$ is an x-periodic function with a period 1. Substituting (A 1) into (2.5) gives

$$\text{Pe}(\tilde{C}_x + \varepsilon \tilde{C}_X) = \tilde{C}_{xx} + 2\varepsilon \tilde{C}_{xX} + \varepsilon^2 \tilde{C}_{XX}, \quad (x \neq n) \tag{A 2a}$$

$$\tilde{C}|_{X=0} = 1, \tag{A 2b}$$

$$\tilde{C}|_{X=1} = 0 \quad \text{or} \quad \tilde{C}|_{X=X_0} = \tilde{C}_X|_{X=X_0} = 0, \quad 0 < X_0 \leq 1, \tag{A 2c}$$

$$\left[\tilde{C}_x + \varepsilon \tilde{C}_X \right]_{x=n} = \text{Da}, \tag{A 2d}$$

for $n = 1, 2, \ldots, N$, setting $X_0 = \varepsilon x_0$ and assuming continuity of $\tilde{C}$ across sinks.

We first address the case $\text{Pe} = O(\varepsilon)$ and $\text{Da} = O(\varepsilon^2)$, setting $\text{Pe} = \varepsilon p$, $\text{Da} = \varepsilon^2 q$ and assuming $p, q = O(1)$ as $\varepsilon \to 0$. We substitute the expansion

$$\tilde{C}(x, X) = C^{(0)}(x, X) + \varepsilon C^{(1)}(x, X) + \varepsilon^2 C^{(2)}(x, X) + \ldots \tag{A 3}$$

into (A 2) and collect terms in powers of ε, assuming the $C^{(i)}$ are $O(1)$ as $\varepsilon \to 0$. At $O(1)$, we find that $C^{(0)} = C^{(0)}(X)$. The homogeneous problem at the following order has the solution $C^{(1)} = 0$. Competition between advection, diffusion and uptake emerges at $O(\varepsilon^2)$, where

$$pC_X^{(0)} = C_{xx}^{(2)} + C_{XX}^{(0)}, \tag{A 4a}$$

$$[C^{(2)}]_{x=0} = 0, \quad [C_x^{(2)}]_{x=0} = q, \quad C^{(2)}|_{X=0} = 0, \tag{A 4b}$$

$$C^{(2)}|_{X=1} = 0 \quad \text{or} \quad C^{(2)}|_{X=X_0} = C_X^{(2)}|_{X=X_0} = 0 \tag{A 4c}$$

It is convenient here to consider a representative unit cell occupying $-\frac{1}{2} < x < \frac{1}{2}$ with the sink at $x = 0$. Averaging (A 4a) over a unit cell, and assuming periodicity of $C_x^{(2)}$, we recover

$$C_{XX}^{(0)} - pC_X^{(0)} = q, \tag{A 5a}$$

$$C^{(0)}|_{X=0} = 1, \quad C^{(0)}|_{X=1} = 0, \tag{A 5b}$$

$$\text{or} \quad C^{(0)}|_{X=0} = 1, \quad C^{(0)}|_{X=X_0} = C_X^{(0)}|_{X=X_0} = 0, \tag{A 5c}$$

for some $0 \leq X_0 \leq 1$. The solution to (A 5) is

$$C^{(0)}(X) = \begin{cases} \left(\frac{q}{p} - 1 \right) \dfrac{e^{pX} - 1}{e^p - 1} - \frac{q}{p} X + 1, & 0 < X < 1, \quad q \leq Q(p) \\ \dfrac{q}{p^2} \dfrac{e^{pX} - 1}{e^{pX_0}} - \frac{q}{p} X + 1, & 0 < X < X_0, \quad q > Q(p) \end{cases} \tag{A 6a}$$

where

$$Q(p) = \frac{p^2 e^p}{(p-1)e^p + 1}, \quad X_0 = -\frac{1}{p} e^{-pX_0} + \frac{q + p^2}{pq}. \tag{A 6b}$$

The internal free boundary at $X = X_0 < 1$ must be considered when the sink strength is large enough for all the solute to be absorbed upstream of $X = 1$. The two-parameter solution (A 6) encompasses four distinct limits (illustrated in Figure 3), denoted D, A, U_D and U_A, in which different effects dominate respec-

tively. On the boundaries between these regions of parameter space we recover one-parameter solutions which capture a balance between two effects. Specifically, diffusion between the boundary source and sink balances advection along $p = O(1)$, $q \ll 1$, where (A 6) reduces to $C^{(0)} \approx 1 - (\mathrm{e}^{pX} - 1)/(\mathrm{e}^p - 1)$, independent of the distributed sinks; diffusion between the boundary source and sinks balances uptake by the distributed sinks along $q = O(1)$, $p \ll 1$, where (A 6) reduces to $C^{(0)} \approx \frac{1}{2}qX^2 - (\frac{1}{2}q + 1)X + 1$ for $q \le 2$, independent of advection; and advection balances uptake by the distributed sinks along $q = O(p)$, $p \gg 1$, where $C^{(0)} \approx 1 - (q/p)X + \mathrm{e}^{-p}((q/p) - 1)(\mathrm{e}^{pX} - 1)$ (for $q \le p$). This limit includes a boundary layer of width $1/p$ near the boundary sink at $X = 1$, across which advection balances diffusion locally. A further balance arises along $q = O(p^2)$, $q \gg 1$, where $q > Q(p)$ and diffusion and advection locally balance uptake (independent of the downstream boundary sink); here $C^{(0)} \approx 1 - (q/p)X + (q/p^2)\mathrm{e}^{-pX_0}(\mathrm{e}^{pX} - 1)$ and $X_0 \approx 2/p$.

Having determined $C^{(0)}$, the second correction $C^{(2)}$ satisfies

$$C^{(2)}_{xx} = -q, \quad [C^{(2)}]_{x=0} = 0, \quad [C^{(2)}_x]_{x=0} = q, \tag{A 7}$$

subject to periodicity over the unit cell and a calibration condition $\langle C^{(2)} \rangle = $ constant, where $\langle f \rangle \equiv \int_{-1/2}^{1/2} f \, \mathrm{d}x$. Thus

$$C^{(2)}(x) = -\frac{q}{2}\left(x^2 - |x| + \frac{1}{6}\right) + \langle C^{(2)} \rangle, \quad (-\tfrac{1}{2} \le x \le \tfrac{1}{2}). \tag{A 8}$$

We impose $C^{(2)}|_{x=0+} = C^{(2)}|_{x=0-} = 0$, so that $C^{(2)}$ satisfies the boundary conditions (A 4b,c), implying that $\langle C^{(2)} \rangle = q/12$. This signals the development of pronounced humps in the concentration profile as q increases. We investigate these by inspecting the second organising centre in parameter space, at $\mathrm{Pe} = O(1)$, $\mathrm{Da} = O(\varepsilon)$.

We set $\mathrm{Pe} = O(1)$ and $\mathrm{Da} = \varepsilon q_1$ with $q_1 = O(1)$ as $\varepsilon \to 0$. Expanding as before using (A 2) and collecting terms in powers of ε, we again find at leading order that $C^{(0)} = C^{(0)}(X)$. At $O(\varepsilon^1)$,

$$C^{(1)}_{xx} - \mathrm{Pe}C^{(1)}_x = \mathrm{Pe}C^{(0)}_X, \tag{A 9a}$$

$$[C^{(1)}]_{x=0} = 0, \quad [C^{(1)}_x]_{x=0} = q_1, \tag{A 9b}$$

$$C^{(1)}|_{X=0} = 0, \quad C^{(1)}|_{X=1} = 0 \text{ or } C^{(0)}|_{X=X_0} = C^{(0)}_X|_{X=X_0} = 0. \tag{A 9c}$$

Averaging (A 9a) over the unit cell, assuming periodicity of $C^{(1)}_x$ and incorporating the jump in $C^{(1)}_x$ at the sink, leads to $\mathrm{Pe}C^{(0)}_X = -q_1$, $C^{(0)}|_{X=0} = 1$, which has the linear solution

$$C^{(0)} = 1 - \frac{q_1}{\mathrm{Pe}}X, \quad (0 \le X < \min(X_0, 1)), \tag{A 10}$$

where $q_1/\mathrm{Pe} \le 1$ if the concentration profile extends to the outlet ($X = 1$), and $q_1/\mathrm{Pe} = 1/X_0$ if the solute concentration drops to zero at $X = X_0 < 1$. In order to satisfy the downstream boundary condition on $C^{(0)}$ at $X = 1$ or $X = X_0$ it is necessary to include a diffusive boundary which is not preserved in this scaling, but which is as described in Regions U_A and A above.

To determine $C^{(1)}$, we note that the source terms $C^{(0)}_X$ and q_1 in the linear

system (A 9a,b) are independent of x, so that superposition may be used to find a solution in the form

$$C^{(1)}(x, X) = -b(x)\text{Pe}C_X^{(0)} + a(x)q_1 = q_1\big(a(x) + b(x)\big), \qquad \text{(A 11)}$$

where $a(x)$ and $b(x)$ are continuous with unit period and satisfy the cell problems $a_{xx} - \text{Pe}\, a_x = 0$, $[a_x]_{0-}^{0+} = 1$, $b_{xx} - \text{Pe}\, b_x = -1$, $[b_x]_{0-}^{0+} = 0$. After some algebra, it follows that

$$C^{(1)}(x) = \frac{q_1}{\text{Pe}}\left(-\frac{\exp\big(\text{Pe}\left(x \pm \tfrac{1}{2}\right)\big)}{2\sinh(\text{Pe}/2)} + x + \frac{2 \pm \text{Pe}}{2\text{Pe}}\right) + \langle C^{(1)}\rangle, \qquad \text{(A 12a)}$$

for $0 < \mp x \le 1/2$. As before, the global boundary conditions (A 9c) are used to derive the local condition $C^{(1)}(0) = 0$, implying

$$\langle C^{(1)}\rangle = \frac{q_1}{2\text{Pe}}\left(\frac{e^{\text{Pe}/2}}{\sinh(\text{Pe}/2)} - \frac{2 + \text{Pe}}{\text{Pe}}\right) = \frac{q_1}{2\text{Pe}}\left(\coth(\text{Pe}/2) - \frac{2}{\text{Pe}}\right), \qquad \text{(A 12b)}$$

therefore $\langle C^{(1)}\rangle \approx \frac{q_1}{2\text{Pe}}(1 - \frac{2}{\text{Pe}})$ at large $\text{Pe} \gg 1$ and $\langle C^{(1)}\rangle \approx \frac{q_1}{12}$ at small $\text{Pe} \ll 1$, so that $C^{(1)}$ in (A 12a) tends to $\varepsilon C^{(2)}$ in (A 8) with error $O(q_1\text{Pe})$. For large Pe, the correction is approximately

$$C^{(1)} = \frac{q_1}{\text{Pe}}\left(x \pm \tfrac{1}{2}\right) + \langle C^{(1)}\rangle + O(\text{Pe}^{-1}), \quad (0 < \mp x \le 1/2) \qquad \text{(A 13)}$$

the discontinuity across the sink being smoothed over a distance (in x) of $1/\text{Pe}$. This gives rise to staircase-like solutions in regions U_2^{s} and A^{s} in Figure 3.

We also observe from (A 12a) that the asymptotic approximation for $\text{Pe} \gg 1$ breaks down when $q_1/\text{Pe} = O(\varepsilon^{-1})$, i.e. $\text{Da} \sim \text{Pe}$, making $\varepsilon C^{(1)}$ of the same order as $C^{(0)}$ in (A 3). Overall, the homogenization approximation applies for $\text{Da} \ll \max(1, \text{Pe})$, as shown in Figure 3($a$).

Appendix B. Homogenization for random sink distributions

When sinks are distributed non-periodically we can derive the homogenized approximation of (2.5) as follows. We focus on the case $\text{Pe} = O(\varepsilon)$, $\text{Da} = O(\varepsilon^2)$, again writing $\text{Pe} = \varepsilon p$ and $\text{Da} = \varepsilon^2 q$. We initially use (A 1) to rewrite (2.5, 2.6) as

$$\tilde{C}_{xx} + 2\varepsilon\tilde{C}_{xX} + \varepsilon^2\tilde{C}_{XX} - \varepsilon p\left(\tilde{C}_x + \varepsilon\tilde{C}_X\right) = \varepsilon^2 qf,$$
$$\tilde{C}|_{X=0} = 1, \quad \tilde{C}|_{X=1} = 0. \qquad \text{(B 1)}$$

(For brevity we assume here that $\tilde{C}$ does not fall to zero upstream of $X = 1$). Expanding using (A 3), we allow $C^{(1)}$ and $C^{(2)}$ to have fluctuations, assuming that these are not large enough to disrupt the proposed expansion. At leading order, $C_{xx}^{(0)} = 0$, $C^{(0)}|_{X=0} = 1$ and $C^{(0)}|_{X=1} = 0$. Thus $C^{(0)}(x, X) = \tilde{A}(X)x + \tilde{B}(X)$ for some $\tilde{A}$ and $\tilde{B}$. The first term must be suppressed to avoid secular growth, so that $C^{(0)} = C^{(0)}(X)$. Likewise at the following order we find that $C^{(1)} = C^{(1)}(X)$.

Collecting the terms in (B 1) at $O(\varepsilon^2)$, we obtain

$$C^{(2)}_{xx} = q(f - F), \quad \text{where} \quad qF(X) \equiv C^{(0)}_{XX} - pC^{(0)}_X, \quad \text{(B 2)}$$

with f given by (2.6). This is to be solved subject to $C^{(1)} = C^{(2)} = 0$ at $x = 0$ and $x = \varepsilon^{-1}$. Thus in $\xi_i < x < \xi_{i+1}$, for $i = 0, 1, 2, \ldots, N$, treating x and X as independent,

$$C^{(2)} = -\tfrac{1}{2}qF(x - \xi_i)^2 + \alpha_i(x - \xi_i) + \beta_i \quad \text{(B 3)}$$

for some α_i, β_i, taking $\xi_0 = 0$ and $\xi_{N+1} = \varepsilon^{-1}$. We define $\Delta_i \equiv \xi_i - \xi_{i-1}$ (for $i = 1, 2, \ldots, N+1$) and $(R_i, S_i, T_i, U_i) \equiv \sum_{j=1}^{i}(\xi_j, \Delta_j^2, \xi_j\Delta_j, \xi_j^2)$ so that $\xi_i \equiv \sum_{j=1}^{i}\Delta_j$ and

$$\sum_{j=1}^{i} \xi_j\xi_{j-1} \equiv U_{i-1} + \tfrac{1}{2}(\xi_i^2 - S_i), \quad \sum_{j=1}^{i} \Delta_j(j-1) \equiv (T_i - R_i) - T_{i-1} = i\xi_i - R_i. \quad \text{(B 4)}$$

Integrating (B 2) across $x = \xi_i$ gives, for $i = 1, 2, \ldots, N$

$$\alpha_i = \alpha_{i-1} + q\left(1 - F\Delta_i\right), \quad \text{(B 5a)}$$

$$\beta_i = \beta_{i-1} - \tfrac{1}{2}qF\Delta_i^2 + \alpha_{i-1}\Delta_i. \quad \text{(B 5b)}$$

We take $\beta_0 = 0$ to satisfy $C^{(2)} = 0$ at $x = 0$. From (B 5), for $i = 1, 2, \ldots, N$,

$$\alpha_i = \alpha_0 + q(i - F\xi_i), \quad \text{(B 6a)}$$

$$\beta_i = -\tfrac{1}{2}qFS_i + \alpha_0\xi_i + q\textstyle\sum_{j=1}^{i}\Delta_j(j - 1 - F\xi_{j-1}). \quad \text{(B 6b)}$$

Substituting (B 6) into (B 3), expanding and using (B 4) gives, after some algebra,

$$C^{(2)} = -\tfrac{1}{2}qFx^2 + \alpha_0 x + q\left[ix - R_i\right] \quad \text{where} \quad \xi_i \leq x < \xi_{i+1}. \quad \text{(B 7)}$$

Imposing $C^{(2)} = 0$ at $x = \varepsilon^{-1} \equiv N + 1$ gives $\alpha_0 = \tfrac{1}{2}qF\varepsilon^{-1} - q\left[N - \varepsilon R_N\right]$, and so

$$C^{(2)} = \tfrac{1}{2}qFx(\varepsilon^{-1} - x) + q\left[x(\varepsilon R_N + i - N) - R_i\right], \quad (\xi_i \leq x < \xi_{i+1}). \quad \text{(B 8)}$$

This expression relates solute fluctuations directly to sink distributions.

When $f = f_n$, then $\xi_i \sim \mathcal{N}(i, \sigma^2) \sim i + \sigma\mathcal{N}(0, 1)$, $\Delta_i \sim \mathcal{N}(1, 2\sigma^2) \sim 1 + \sqrt{2}\sigma\mathcal{N}(0, 1)$ and $R_i \sim \tfrac{1}{2}i(i+1) + \sigma\sqrt{i}N(0, 1)$. To evaluate the distribution of $\varepsilon x R_N -$

R_i we must sum independent distributions. Setting $x = X/\varepsilon$,

$$XR_N - R_i = X\sum_{j=1}^{N}\xi_j - \sum_{j=1}^{i}\xi_j = (X-1)\sum_{j=1}^{i}\xi_j + X\sum_{j=i+1}^{N}\xi_j$$

$$\sim(X-1)\sum_{j=1}^{i}\mathcal{N}(j,\sigma^2) + X\sum_{j=i+1}^{N}\mathcal{N}(j,\sigma^2)$$

$$\sim(X-1)\mathcal{N}\left(\tfrac{1}{2}i(i+1),\sigma^2 i\right) + X\mathcal{N}\left(\tfrac{1}{2}N(N+1) - \tfrac{1}{2}i(i+1),\sigma^2(N-i)\right)$$

$$\sim\mathcal{N}\left(\tfrac{1}{2}N(N+1)X - \tfrac{1}{2}i(i+1),\sigma^2[i(X-1)^2 + (N-i)X^2]\right)$$

$$\sim\varepsilon^{-2}\mathcal{N}\left(\tfrac{1}{2}X(1-X),\sigma^2\varepsilon^3 X(1-X)\right) + \dots$$

writing $i = (X/\varepsilon) + (i-x)$, retaining $(i-x)$ as an $O(1)$ quantity. We therefore find from (B 8) that (after some algebra), for $\xi_i \leq x < \xi_{i+1}$,

$$\mathbb{E}(C^{(2)}) = \tfrac{1}{2}\frac{q}{\varepsilon^2}(F-1)X(1-X) + \tfrac{1}{2}q(x-i)(i+1-x). \tag{B 9}$$

To ensure the original expansion is asymptotic, we must therefore take $F = 1$ at $O(\varepsilon^{-2})$, yielding (A 5a) for $C^{(0)}$. Simulations indicate that the contribution at $O(\varepsilon^{-1})$ (and hence $C^{(1)}$) vanishes. Similarly we find that

$$\mathrm{Var}(C^{(2)}) = \varepsilon^{-1}\sigma^2 q^2 X(1-X) + O(1), \tag{B 10}$$

in agreement with simulations (not shown). $\mathrm{Cov}_T(C^{(2)})$ can be determined in a similar manner. Thus while $C^{(2)}$ has $O(1)$ mean, r^ε is dominated by fluctuations of relative magnitude $O(\varepsilon^{3/2})$. This approximation holds as long as sinks do not exchange places, which can be expected once σ becomes sufficiently large. (B 10) suggests that the fluctuations in the case of stronger mixing of sink locations will be larger than $O(\varepsilon^{3/2})$.

When $f = f_u$, we turn to Matuswana [29], who determined the distribution of linear combinations of order statistics drawn from $\mathcal{U}(0,1)$ (i.e. combinations of $\hat{\xi}_1, \hat{\xi}_2, \ldots, \hat{\xi}_N$, where $\hat{\xi}_i \equiv \varepsilon\xi_i$) as a mixture of scaled Beta distributions. Writing $L_N = \sum_{i=1}^{N} a_i\hat{\xi}_i$ for some a_i, and defining $b_j = \sum_{i=j}^{N} a_i$, L_N has mean and variance

$$\frac{\sum_{j=1}^{N} b_j}{N+1} \quad\text{and}\quad \frac{\sum_{j=1}^{N} b_j^2}{(N+1)(N+2)} - \frac{\left(\sum_{j=1}^{N} b_j\right)^2}{(N+1)^2(N+2)} \tag{B 11}$$

respectively [29]. Writing $\hat{R}_i = \sum_{j=1}^{i}\hat{\xi}_j$ and setting $L_N = X\hat{R}_N - \hat{R}_i$ we have $a_j = X - 1$ for $1 \leq j \leq i$ and $a_j = X$ for $i+1 \leq j \leq N$, and hence

$$b_j = \begin{cases} (X-1)(i-j+1) + X(N-i) & (1 \leq j \leq i), \\ X(N-j+1) & (i+1 \leq j \leq N). \end{cases} \tag{B 12}$$

Evaluating appropriate sums of b_j and again writing $x = X/\varepsilon$, $i = (X/\varepsilon) + (i-x)$ (taking $|i-x| = O(1)$), we find to leading order in ε using (B 11) that $XR_N - R_i$

has mean and variance

$$\tfrac{1}{2}\varepsilon^{-2}X(1-X) \quad \text{and} \quad \tfrac{1}{12}\varepsilon^{-3}X^2(1-X)^2 \qquad (B\,13)$$

respectively. We thereby recover (B 9) (after some algebra), requiring that $F = 1 + O(\varepsilon)$, so once more $C^{(0)}$ satisfies (A 5a). Furthermore, assuming $\mathrm{Var}(C^{(1)}) = 0$, we obtain $\mathrm{Var}(r^\varepsilon) = \tfrac{1}{12}q^2\varepsilon X^2(1-X)^2$ to leading order in ε, consistent with simulations. Thus fluctuations about $C^{(0)}$ are $O(\varepsilon^{1/2})$. Furthermore, simulations show that $\mathbb{E}(r^\varepsilon) \approx \tfrac{1}{2}\varepsilon q X(1-X)$, suggesting a contribution from $C^{(1)}$ which presumably must be determined by a closure condition at higher order.

Acknowledgements

References

[1] Moffett, A. & Loke, C. 2006 Immunology of placentation in eutherian mammals. *Nature Rev. Immunol.* **6**, 584–594. (doi:10.1038/nri1897)

[2] Kaufmann, P. & Scheffen, I. 1992 *Fetal and Neonatal Physiology*, vol. 1, ch. Placental Development, pp. 47–56. Philadelphia: Saunders.

[3] Mayhew, T. M., Charnock-Jones, D. S. & Kaufmann, P. 2004 Aspects of human fetoplacental vasculogenesis and angiogenesis. III. Changes in complicated pregnancies. *Placenta* **25**, 127–139. (doi:10.1016/j.placenta.2003.10.010)

[4] Leach, L., Gray, C., Staton, S., Babawale, M. O., Gruchy, A., Foster, C., Mayhew, T. M. & James, D. K. 2004 Vascular endothelial cadherin and β-catenin in human fetoplacental vessels of pregnancies complicated by Type 1 diabetes: associations with angiogenesis and perturbed barrier function. *Diabetologia* **47**, 695–709. (doi:10.1007/s00125-004-1341-7)

[5] Leach, L., Taylor, A. & Sciota, F. 2009 Vascular dysfunction in the diabetic placenta: causes and consequences. *J. Anat.* **215**, 69–76. (doi:10.1111/j.1469-7580.2009.01098.x)

[6] Chernyavsky, I. L., Jensen, O. E. & Leach, L. 2010 A mathematical model of intervillous blood flow in the human placentone. *Placenta* **31**, 44–52. (doi:10.1016/j.placenta.2009.11.003)

[7] Erian, F. F., Corrsin, S. & Davis, S. H. 1977 Maternal, placental blood flow: A model with velocity-dependent permeability. *J. Biomech.* **10**, 807–814. (doi:10.1016/0021-9290(77)90095-1)

[8] Schmid-Schönbein, H. 1988 Conceptional proposition for a specific microcirculatory problem: maternal blood flow in hemochorial multivillous placentae as percolation of a "porous medium". *Trophoblast Res.* **3**, 17–38.

[9] Bensoussan, A., Lions, J.-L. & Papanicolaou, G. 1978 *Asymptotic analysis for periodic structures*, *Studies in mathematics and its applications*, vol. 5. Elsevier North-Holland.

[10] Bakhvalov, N. S. & Panasenko, G. P. 1989 *Homogenisation: averaging processes in periodic media : mathematical problems in the mechanics of composite materials*, *Mathematics and its applications*, vol. 36. Dordrecht; Boston: Kluwer Academic Publishers.

[11] Pavliotis, G. A. & Stuart, A. M. 2008 *Multiscale methods: Averaging and homogenization*, *Texts in Applied Mathematics*, vol. 53. Springer.

[12] Torquato, S. 2006 *Random heterogeneous materials: Microstructure and macroscopic properties*, *Interdisciplinary Applied Mathematics*, vol. 16. Springer, corr. 2nd printing edn.

[13] Mei, C. C. & Auriault, J.-L. 1991 The effect of weak inertia on flow through a porous medium. *J. Fluid Mech.* **222**, 647–663. (doi: 10.1017/S0022112091001258)

[14] Burridge, R. & Keller, J. B. 1981 Poroelasticity equations derived from microstructure. *J. Acoust. Soc. Am.* **70**, 1140–1146. (doi:10.1121/1.386945)

[15] Shipley, R. J. & Chapman, S. J. 2010 Multiscale modelling of fluid and drug transport invascular tumours. *Bull. Math. Biol.* **72**, 1464–1491. (doi: 10.1007/s11538-010-9504-9)

[16] Whitaker, S. 1999 *The Method of Volume Averaging*. Dordrecht: Kluwer Academic Publishers.

[17] Rubinstein, J. & Torquato, S. 1989 Flow in random porous media: mathematical formulation, variational principles, and rigorous bounds. *J. Fluid Mech.* **206**, 25–46. (doi:10.1017/S0022112089002211)

[18] Bourgeat, A. & Piatnitski, A. 1999 Estimates in probability of the residual between the random and the homogenized solutions of one-dimensional second-order operator. *Asymp. Anal.* **21**, 303–315.

[19] Bal, G., Garnier, J., Motsch, S. & Perrier, V. 2008 Random integrals and correctors in homogenization. *Asymp. Anal.* **59**, 1–26. (doi:10.3233/ASY-2008-0890)

[20] Sangani, A. S. & Acrivos, A. 1982 Slow flow past periodic arrays of cylinders with application to heat transfer. *Int. J. Multiph. Flow* **8**, 193–206. (doi: 10.1016/0301-9322(82)90029-5)

[21] Mauri, R. 1991 Dispersion, convection, and reaction in porous media. *Phys. Fluids A* **3**, 743–756. (doi:10.1063/1.858007)

[22] Mikelić, A., Devigne, V. & van Duijn, C. J. 2006 Rigorous upscaling of the reactive flow through a pore, under dominant Péclet and Damköhler numbers. *SIAM J. Math. Anal.* **38**, 1262–1287. (doi:10.1137/050633573)

[23] Allaire, G. & Raphael, A.-L. 2007 Homogenization of a convection-diffusion model with reaction in a porous medium. *Comp. Ren. Math.* **344**, 523–528. (doi:10.1016/j.crma.2007.03.008)

[24] Rainey, A. & Mayhew, T. M. 2010 Volumes and numbers of intervillous pores and villous domains in placentas associated with intrauterine growth restriction and/or pre-eclampsia. *Placenta* **31**, 602–606. (doi:10.1016/j.placenta.2010.04.005)

[25] Diggle, P. J. 2003 *Statistical Analysis of Spatial Point Patterns.* London: Arnold, 2nd edn.

[26] Papadopulos, F., Spinelli, M., Valente, S., Foroni, L., Orrico, C., Alviano, F. & Pasquinelli, G. 2007 Common tasks in microscopic and ultrastructural image analysis using ImageJ. *Ultrastruct. Path.* **31**, 401–407. (doi:10.1080/01913120701719189)

[27] Lotwick, H. W. & Silverman, B. W. 1982 Methods for analysing spatial processes of several types of points. *J. R. Stat. Soc. B* **44**, 406–413.

[28] Baddeley, A. & Turner, R. 2005 Spatstat: an R package for analyzing spatial point patterns. *J. Stat. Software* **12**, 1–42. URL: `www.jstatsoft.org`, ISSN: 1548-7660.

[29] Matsunawa, T. 1985 The exact and approximate distributions of linear combinations of selected order statistics from a uniform distribution. *Ann. Inst. Stat. Math.* **37**, 1–16. (doi:10.1007/BF02481076)

[30] Stoyan, D., Kendall, W. S. & Mecke, J. 1995 *Stochastic Geometry and its Applications.* Ann Arbor, MI: UMI, 2nd edn.

[31] Bernardo, J. M. & Smith, A. F. M. 1993 *Bayesian Theory.* Wiley, Chichester.

[32] Holmes, M. H. 1998 *Introduction to Perturbation Methods*, *Texts in Applied Mathematics*, vol. 20. Springer. Corr. 2nd printing.

[33] Taylor, C. C., Dryden, I. L. & Farnoosh, R. 2001 The K-function for nearly regular point processes. *Biometrics* **57**, 224–231. (doi:10.1111/j.0006-341X.2001.00224.x)

[34] Sengers, B. G., Please, C. P. & Lewis, R. M. 2010 Computational modelling of amino acid transfer interactions in the placenta. *Exp. Physiol.* **95**, 829–840. (doi:10.1113/expphysiol.2010.052902)

[35] Auriault, J. L. & Adler, P. M. 1995 Taylor dispersion in porous media: Analysis by multiple scale expansions. *Adv. Water Res.* **18**, 217–226. (doi:10.1016/0309-1708(95)00011-7)

[36] Bonfiglio, A., Leungchavaphongse, K., Repetto, R. & Siggers, J. H. 2010 Mathematical modeling of the circulation in the liver lobule. *J. Biomech. Engng* **132**, 111011. (doi:10.1115/1.4002563)